POAC'13
Espoo, Finland

Proceedings of the 22nd International Conference on
Port and Ocean Engineering under Arctic Conditions
June 9-13, 2013
Espoo, Finland

Rubble Ice Transport on Arctic Offshore Structures (RITAS), part IV: Tactile sensor measurement of the level ice load on inclined plate

Wenjun Lu[1], Nicolas Serre[2], Knut Høyland[1] and Karl-Ulrich Evers[3]

[1)]SAMCoT, NTNU, Trondheim, Norway

[2)]Multiconsult, Tromsø, Norway

[3)]Hamburg Ship Model Basin (HSVA), Hamburg, Germany

wenjun.lu@ntnu.no

ABSTRACT

When level ice interacts with downward wide sloping structures, the incoming level ice usually fails in bending failure mode. As the failed rubble accumulates, the bending process is influenced by the rubble beneath. An experimental investigation of the effect from the volume-growing rubble field in front of a sloping structure is described in the present paper. It is completed by 3 associated papers: "*Rubble Ice Transport on Arctic Offshore Structures (RITAS), part I: Model scale investigation of level ice action mechanisms*", "*Part II: 2D model scale study of the level ice action*", and "*part III: Analysis of model scale rubble ice stability*". The present paper describes an experiment where we have mounted a tactile sensor on the sloping surface of a structure measuring the ice pressure's spatial and temporal variation. As oppose to the ice load measured at the waterline, it is found out that equally large ice load was also detected below waterline region. This is postulated due to the contribution from the ice rotating process. Especially, as the accumulated rubble's volume grows, the load induced by the ice rotating process and static rubble pressure increase significantly and eventually changes the ice bending process.

Introduction

Wide sloping structures have many applications in the ice infested waters. Due to the relatively limited ice clearing capability of a wide sloping structure, the presence of rubble greatly influences the whole interaction mechanism (Serré et al., 2013a). The significance of the rubble accumulation has been investigated in the current test set-up as a preparation for a new theoretical model. The current paper focuses on the test set-up and results. Its layouts are as in the following: First, the test set-up and test matrix are briefly introduced. Additional information is given in (Serré et al., 2013a). Following this, the installation and calibration of the tactile sensor are presented into detail. Then the ice load's spatial and temporal variations during ice structure interaction and rubble accumulation are presented. Lastly, based on the discussion made on the measured data, the interaction mechanisms are discussed and important findings are concluded.

Test set-up

The physical tests are conducted in the ice tank at the Hamburg Ship Model Basin (HSVA). The geometry of the test set-up and the location where the tactile sensor is mounted are shown in Figure 1. During the tests, the Tekscan sensor #5513 was utilized. It has an operating temperature ranging from -9 ^{o}C to 60 ^{o}C; the pressure measuring range was claimed to be within 0 to 175 MPa. All these specifications are compatible with the current application. Most importantly, this sensor has a rather long tail. This ensures that the handle which connects the tail to the computer can be positioned far away from the water.

The tactile sensor is mounted in the center of the sloping plate. Due to limited size of the sensor, the plate is only partially covered, as shown in Figure 1 (c). The sensor was positioned in the upper middle part of the sloping plate. It is positioned in such a way that 1/3 of the measuring area is above the waterline while the remaining 2/3 of the measuring area is below the waterline. The tactile sensor is composed of 44×55 sensels which are used to measure the local load and averaged into each small sensel as pressure. The ice load's spatial resolution is determined by the size of each sensel as shown in Figure 1 (c). Temporally, the sensor is scanning at a frequency of 10 Hz during each experiment. There are two reasons for using this scanning frequency. For one reason, the interaction speed is usually very low. The main focus of this research is the bending failure of ice and also the rubble accumulation load. Both of them are of rather low frequency in comparison to the continuous crushing process. Therefore a 10 Hz scanning frequency is considered enough to capture the concerned load information; for another reason, utilization of such a lowered frequency is mainly to ensure that the storage capacity during each measurements campaign.

Test matrix

There are in total 5 ice sheets prepared and the box is pushed within each ice sheet with different speeds. The test matrix is shown in Table 1 together with the ice properties in model scale.

Tactile sensor installation

As recommended in the manual (Tekscan, 2011), during the installation, great attention has been paid to make sure the tactile sensor is waterproof and protected from ice abrasion during the test.

With respect to the waterproof issue, similar as previous experimental practices (Määttänen et al., 2012), the tactile sensor is protected by two waterproof layers (plastic film) adhered by

silicone gel. However, during the experiment, a small amount of water eventually entered into the plastic film bag and had contact with the sensor. After each test, the sloping plate is dismantled, cleaned with fresh water and dried under room temperature.

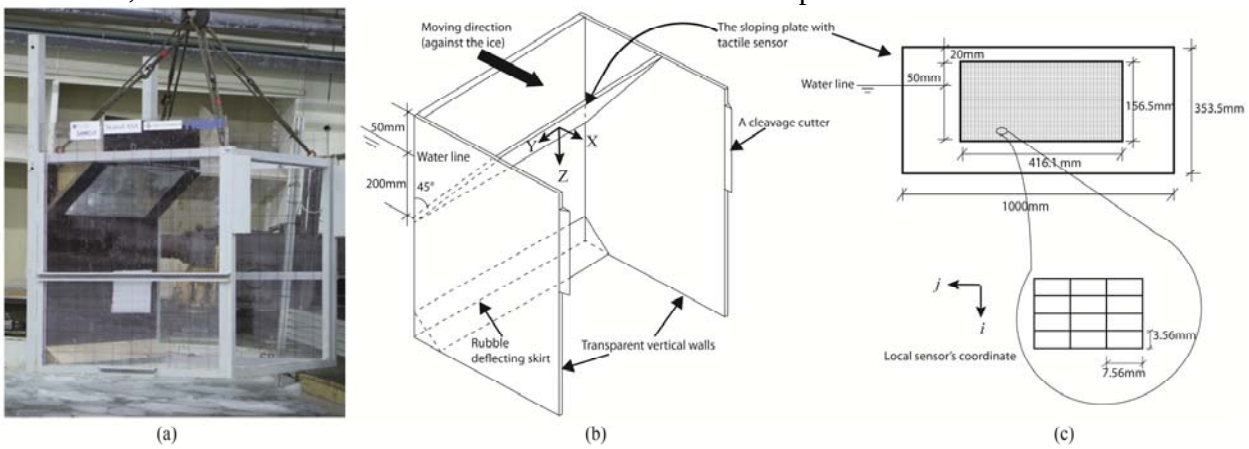

Figure 1 (a) The buoyancy box (b) The schematic drawing of the test set-up with geometry (N.B, drawing not in scale) (c) The tactile sensor.

Table 1 The test matrix

Test series	flexural strength	Ice thickness	Young's Modulus	Speed	Travelling distance
1210	53 kPa	0.043 m	61 MPa	0.045 m/s	10 m
2210	58.2 kPa	0.043 m	53 MPa	0.2 m/s	20 m
3210	54.6 kPa	0.047 m	88 MPa	0.045 m/s	10 m
3211	54.6 kPa	0.047 m	88 MPa	0.2 m/s	10 m
3212	54.6 kPa	0.047 m	88 MPa	0.045 m/s	10 m
4210	45.7 kPa	0.061 m	103 MPa	0.02 m/s	10 m
4211	45.7 kPa	0.061 m	103 MPa	0.2 m/s	10 m
4212	45.7 kPa	0.061 m	103 MPa	0.045 m/s	10 m
5210	47.1 kPa	0.041 m	31 MPa	0.045 m/s	10 m

Table 2 Validation of the tactile sensor with known weights before each test

	Validation weight [kg]	Measured weight [N]	Error
Test 2210	25	260	4%
	25	280	12%
	25	272	8%
Test 321x (x=0,1,2)	20	198-200	1%
	25	265	4%
	10	105	5%
Test 421x (x=0,1,2) and 5210	5	54	8%
	10	100	0%
	15	142	5%
	20	222	11%

Before each test, the tactile sensor is again validated against several known weights so as to confirm its functionality (the detailed procedures and methods are introduced in the next

section). In all the validations, the errors between the measured results and the known weights were all within 15% as shown in Table 2. In terms of the ice abrasion protection, a thin adhesive metallic foil was selected. This metallic foil is 0.15 mm thick and its strength was tested by crushing several cold fresh water ice blocks onto it without causing visual damage.

In conclusion, the installation of the tactile sensor on the sloping plate includes the following important steps corresponding to Figure 2:

(1) The sensor was first put in between two plastic films adhered by silicone gel so as to make it waterproof.

(2) The metallic adhesive layer was applied above the sensor serving as the abrasion protection.

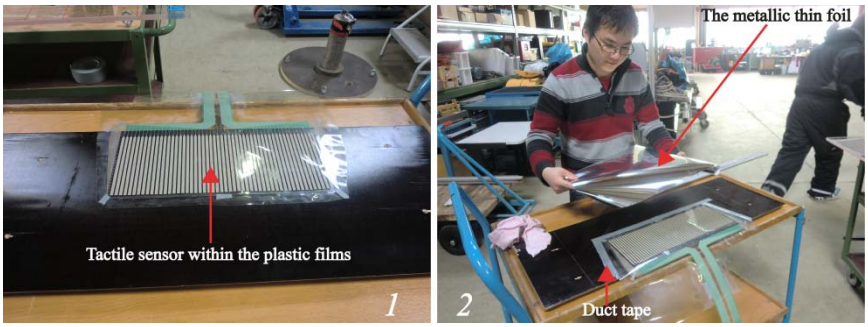

Figure 2 Installation of the tactile sensor on the sloping plate.

Tactile sensor calibration

After the installation of the tactile sensor, a 2 point method was utilized to calibrate the tactile sensor with different sensitivities (Tekscan, 2003). The calibrations and also the above mentioned validations were all conducted in the cold room with temperature around 0 ^{o}C which is rather close to the ice temperature (e.g. -0.6 ~ -0.8 ^{o}C). During the calibration/validation[1], a rubber pad (150 mm × 100 mm × 5 mm, with negligible weight) was utilized to transfer the deadweight to the tactile sensor. This rubber pad usually is randomly placed within the tactile sensor to make a location-blind calibration/validation. Due to the surface roughness both on the rubber pad, on the deadweight, and also on the wooden plate onto which the tactile sensor was attached, the contact area varies slightly in each calibration/validation. It is worth noting here that since the equilibrator with which to eliminate the tactile sensor measurement's spatial errors was unavailable, no further effort was made to confirm the tactile sensor's accuracies in spatial measurement in all the calibrations/validations. It was simply assumed here that the measured load's spatial variation is trustworthy.

The outputs of the ice pressure contour are illustrated by different color bands. A proper saturation pressure is such that the ice pressure contour covers as much color band as possible (see Figure 3 (c)) without exceeding the measuring range (e.g. Figure 3 (a) and Figure 3 (b)). However, in the current test, the interest lies in the local ice pressure for the bending failure mode of ice sheets. Previous applications of tactile sensor in ice load measurements were mainly conducted in ice crushing scenarios (Määttänen et al., 2012; Sodhi, 2001; Sodhi et al.,

[1] This section is dedicated to the calibration method of the tactile sensor used in this test. However, its procedure and methods share several commons with the previously mentioned validation of the tactile sensor (see Table 2). They are introduced here together with the expression 'calibration/validation' if they share a common feature.

1998). The potential local ice pressure in the current test setting is therefore not known a priori. Accordingly, several rounds of trial and errors were made to make sure the chosen sensitivity and saturation pressure can properly yield a 'colorful' output of the ice load pressures as shown in a sample ice pressure outputs in Figure 3 (d)). Eventually, a much lower saturation pressure is adopted in the current test comparing to previous applications as shown in Table 3.

However, it is worth noting that the tactile sensor does not have the same accuracy in all the pressure range (Tekscan, 2003). This can also be seen from the validation measurements shown in Table 2. This nonlinear nature has been discussed in (Izumiyama et al., 1999). Due to the complexity of ice and structure interactions, the ice pressure covers a very wide range of possible values. In the current tests, based on the chosen sensitivity and saturation pressure, the tactile sensor tends to capture the ice pressure that repeats most often, saying the pressure that would be around the mean ice pressure. However, for extreme values, the sensor is prone to underestimate the extreme values. It is not possible now to quantify how much the extreme values have been underestimated. Even though, the merits of using tactile sensor in the current test should not be degraded. The tactile sensor will anyhow output the contact area (i.e. the load's spatial variation) and comparative pressure irrespective of possible errors within its measured maximum values.

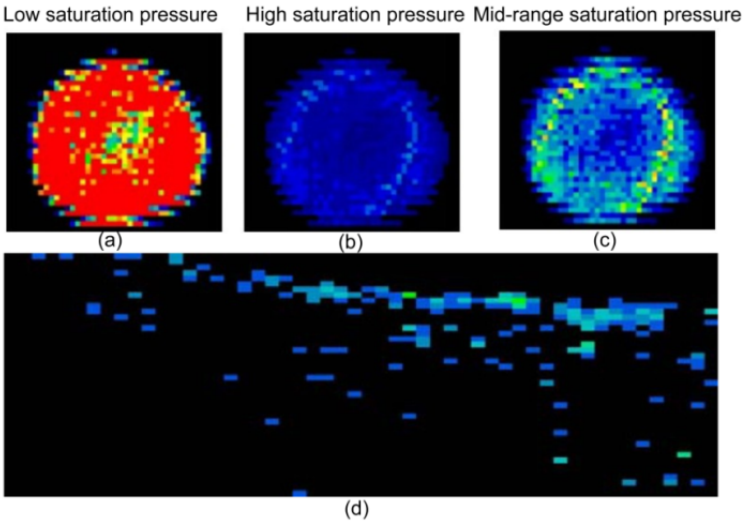

Figure 3 Measurements with different saturations (a),(b)and (c); and a sample of current ice pressure measurements(d). (figures (a),(b) and (c) are from user's manual of Tekscan (2003)).

Table 3 Sensitivity and saturation pressure of the tactile sensor

	Saturation pressure	Sensitivity	Application
(Sodhi et al., 1998)	6.86 MPa	unknown	sea ice crushing failure (full scale)
(Määttänen et al., 2012)	1.6 Mpa 4.5 Mpa	30 23	Salty ice crushing failure (not scaled)
(Kim, 2012)	20 Mpa 6 Mpa 8-10 Mpa	13 13 13	Fresh water ice crushing failure (model scale)
Current test	125 kPa	40	Salty ice bending failure (model scale)

Experimental observation

The visual observations are introduced here as a preparation for future discussion. The general interaction procedure can be illustrated as in Figure 4 (a), (b) and (c). Initially the incoming ice fails in bending against the downward sloping plate (see Figure 4 (a)). Afterwards, this broken ice piece is further rotated downwards (Figure 4 (b)). This ice rotating process is further illustrated in Figure 4 (d) from a side view. It can be seen that there leaves a gap between the sloping plate and the incoming ice. This rotating ice is supposed to transfer the ice load downwards lower than the waterline. As the interaction proceeds, more ice rubbles accumulate beneath the incoming ice (see Figure 4 (e)). The rubble accumulation's track is illustrated by the arrows in Figure 4 (e). This volume-growing ice rubble tends to shift the failing mechanism of the incoming ice sheet from 'bending downwards by the structure' to 'bending upwards by the accumulated rubbles' as shown in Figure 4 (c).

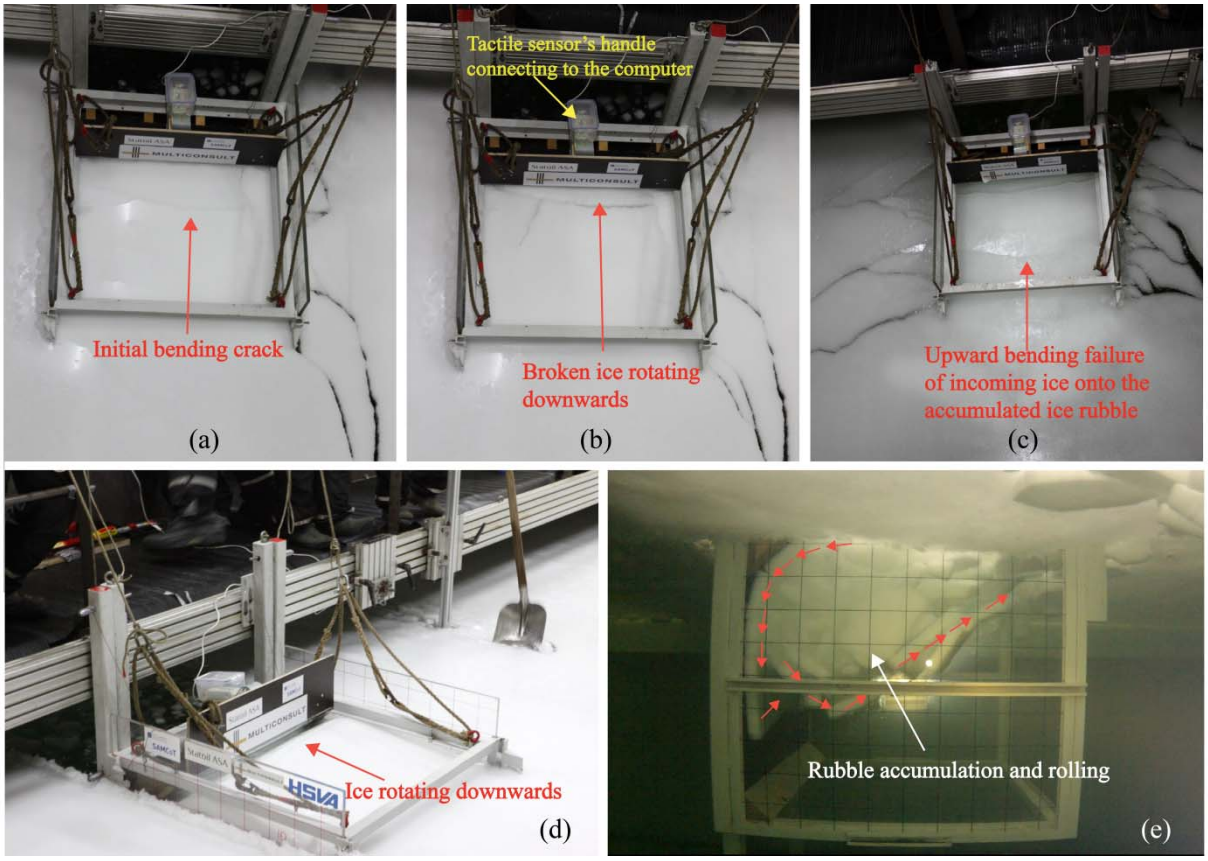

Figure 4 (a), (b) and (c) the interaction procedures; (d) the ice rotating side view; (e) the rubble accumulation.

Experimental results

An example of the measured local normal pressure is shown in Figure 5 (different colors represent different pressure magnitude). This measurement illustrates one circle of the ice load development (i.e. ice breaks at the waterline and slides downwards afterwards). It takes approximately 3 seconds for such cycle to develop in Test 1210. It can be seen that the pressures are not uniform in the lateral Y direction, meaning that non-uniform contact is taking place[2]. Furthermore, after the initial breaking of the incoming ice, the local pressure

[2] Since this is just a random case illustrating the visualization of the ice load development, dissimilar trend in comparison to Figure 6 is possible.

did not diminish instantly. Instead, the pressure keeps travelling down at a relatively smaller yet comparable magnitude.

All these recorded normal pressures are later multiplied with the sensel's area and projected in the horizontal direction (opposite of X direction). They were stored as a third order tensor **M** with components $M_{ijk.}$ Here i and j represent the row and column numbers of the tactile sensor's sensel. And k is the number of scans, representing the recording time.

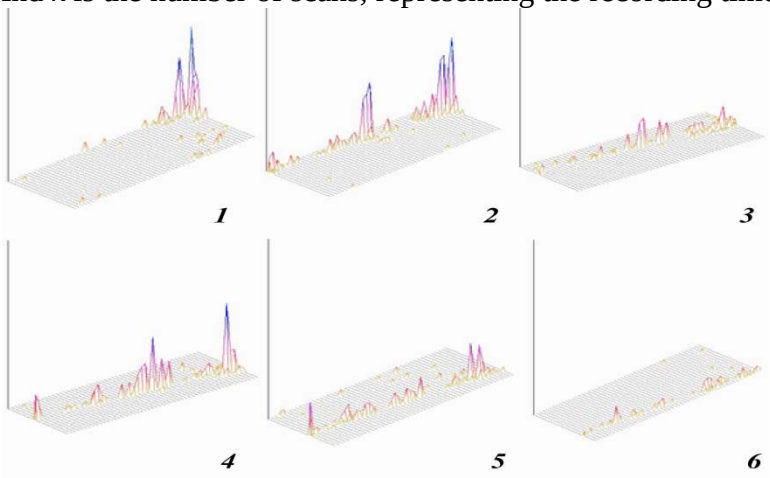

Figure 5 A real time display of the pressure evolution.

Measurements of ice load's spatial variation

It is firstly decided to show how the load varies in the lateral direction (Y or j direction). Therefore, M_{ijk} is processed as in the following:

$$\bar{H}_j = \frac{1}{n_k}\sum_{k=1}^{n_k}[\frac{1}{n_i}(\sum_{i=1}^{n_i} M_{ijk})] \qquad [\,1\,]$$

$$H_{j,max} = \max_{1\le k\le n_k}[\frac{1}{n_i}(\sum_{i=1}^{n_i} M_{ijk})] \qquad [\,2\,]$$

In the previous two equations [1] and [2], the recorded value M_{ijk} is first averaged in the vertical i direction, and then the corresponding time domain (i.e. k direction) averaged lateral load distribution $\bar{H}_j$ and maximum value $H_{j,max}$ are obtained as shown in Figure 6.

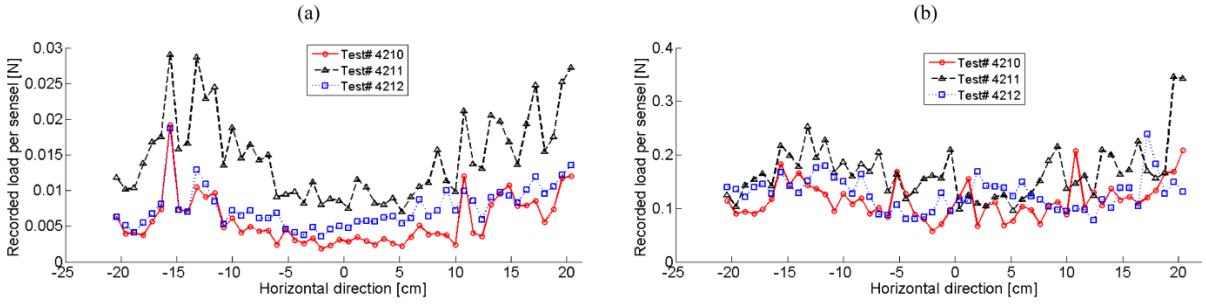

Figure 6 (a) Mean ice load (in time history) and (b) Max ice load (in time history) in the lateral directions of the sensor.

Then the load variation in the vertical direction is investigated with the following equation

$$\bar{V}_j = \frac{1}{n_k}\sum_{k=1}^{n_k}\left(\sum_{j=1}^{n_j} M_{ijk}\right) \qquad [3]$$

$$V_{j,max} = \max_{1\le k\le n_k}\left[\left(\sum_{j=1}^{n_j} M_{ijk}\right)\right] \qquad [4]$$

The comparison of $\bar{V}_j$ and $V_{j,max}$ in different location Z (the distance from the upper side of the tactile sensor) for test 1210 are shown in Figure 7's left column and right column respectively. Together shown in the figure is also the location of the un-deformed level ice. The results in other tests show similar variation trend in the vertical direction (Lu et al., 2013a).

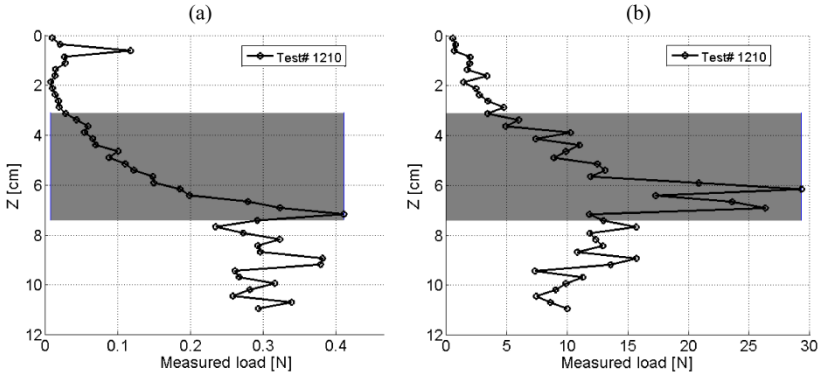

Figure 7 (a) The mean ice load (in time history) and (b) the maximum ice load (in time history) variation in the vertical direction of the sensor (the shaded area is the location of the un-deformed level ice).

Discussions about ice load's spatial variation

It can be seen from the Figure 6 that in the lateral direction, comparing to the maximum load, the mean load varies significantly in different lateral locations. The recorded mean loads are always larger in both lateral sides of the sloping plate (i.e. lateral location around -15.0 cm and 15.0 cm) than in the middle (i.e. lateral location around 0.0 cm). There might be two explanations to such uneven lateral mean load distribution. First, this is due to the non-uniform contact between the incoming level ice and the sloping plate (also can be seen in Figure 5); Secondly, this is due to the tactile sensor's measuring error under the possibilities that the tactile sensor does not have the same sensitivity in all its sensels. The equilibration procedure (Tekscan, 2003) to ensure all the sensels having the same sensitivity was not conducted in the current test due to the lack of equipment. However, the user's manual claims that there exists only slight variations within individual sensels (Tekscan, 2011).

Between the above mentioned two explanations, the authors are prone to adopt the first non-uniform contact explanation for the following three reasons. Firstly, non-uniform contact is taking place throughout the whole experiment as shown by the measurements in Figure 4 (a), (b), and Figure 5. Secondly, in the lateral direction, during the bending process, the incoming ice suffers more boundary confinement on both lateral sides. This can lead to more frequent larger bending force on both lateral sides than in the middle. Though it might be argued that the sensor covers only a small portion of the inclined plate situating in the centre; therefore the boundary effects are negligibly influencing the shoulders of the sensor. However, as can be seen from Figure 4 (a) and (b), the boundary effects really leads to additional 'radial' cracks which locate rather close to the centre. This illustrates how much the boundary effects can propagate inward and eventually influence the ice bending load. Thirdly, if there are large

differences in the sensitivity of sensels in the lateral direction, both the maximum and mean load should be amplified at the same sensitive locations. On the contrary here, the maximum recorded load shows less lateral location variation as shown in the lower figure of Figure 6. This helps to exclude the existence of large difference in the sensels' sensitivity.

Based on the above discussion, in order to quantify the influence of the non-uniform contact, a variation factor is defined here as:

$$k_v = \frac{\sigma}{\mu} \qquad [5]$$

σ is the standard deviation of the measurements of $\bar{H}_j$ or $H_{j,max}$

μ is the mean value of $\bar{H}_j$ or $H_{j,max}$

Perfectly even contact and uniform breaking of homogeneous ice would yield $k_v = 0$. However, the presence of non-uniform contact in all the experiments leads to the value of k_v as shown in Table 4.

Table 4 Variation factor of different test series

Test series	k_v of $\bar{H}_j$	k_v of $H_{j,max}$
1210	0.54	0.42
2210	0.45	0.31
3210	0.65	0.39
3211	0.35	0.25
3212	0.37	0.30
4210	0.60	0.29
4211	0.40	0.31
4212	0.39	0.25
5210	0.53	0.34

It can be seen from Table 4 that non-uniform contact takes place for all experiments. And as discussed before, the maximum values are not as much influenced by non-uniform breaking as those of mean values.

With respect to the ice load's vertical direction variations, both elastic foundation beam and plate theory suggest that the tip deflection at flexural failure (see Figure 4 (a)) is minimal comparing to the thickness of the ice. Therefore, it would be reasonable to assume the ice breaking load (i.e. the load required to bend the incoming intact ice) is within the un-deformed level ice's thickness region (i.e. the shaded area in Figure 7). Note that inside this region, other interaction mechanisms such as the initial ice rotating and rubble effect also exit (Lu et al., 2013a).

It is observed in Figure 7 (b) that the maximum load of $V_{j,max}$ are mainly found within such shaded area. This agrees with our common sense and previous research assumptions that the ice breaking load is one of the decisive components of the ice load. However, as it is shown in the theoretical model (Lu et al., 2013a; Lu et al., 2013b), the ice rotating load would also become decisive when there is sufficient rubble accumulated in front of the structure. For the time being, it can be simply concluded that based on the tactile sensor's measurement, the maximum load often takes place around the un-deformed level ice's thickness region. This is

in agreement with the measurements conducted by Timco (1991) with a similar test set-up within broken ice field. The numerical simulation conducted by Paavilainen and Tuhkuri (2013) also detected the maximum ice load slightly below the waterline for gentle sloping angles.

On the other hand, it is shown in Figure 7 (a) that, the mean load $\bar{V}_j$ usually keeps increasing, or at least stays in a same level, even after passing the shaded area. This is to say, some other equally profound interaction mechanisms other than ice breaking process are taking place below the shaded area. If categorizing the ice sloping structure interaction process as those in ice ship interactions (Kotras, 1983; Lindqvist, 1989; Valanto, 2001), it is speculated that the ice rotating load (i.e. the load required to rotate the already broken ice rubble paralleling to the sloping surface) is the reason for such undiminishing mean load on the sensor below the shaded area. This ice rotating load is introduced by the ice rotating process as shown in Figure 4 (b) and (d). Additional ice load is needed to rotate the already broken ice downwards. This rotating process further transferred the ice load beneath the shaded area (i.e. the un-deformed level ice thickness region) in Figure 7.

Results of ice load's temporal variation

The measured local ice load is summed in both *i* and *j* directions as in equation [6] and displayed in Figure 8. The whole loading histories of all tests presents a cyclic pattern. In order to identify the ice load's temporal variation, the loading history (i.e. ice penetration) is sectionalized by the ice breaking length L_B (see equation [7]). This ice breaking length can be determined by the static solutions of an elastic-foundation beam. Afterwards the mean load and maximum load measured inside each of such section is calculated so as to identify the ice load's temporal evolution (e.g. as illustrated in Figure 8 (a)).

$$F_{k,total} = \sum_{i=1}^{n_i} \sum_{j=1}^{n_j} M_{ijk} \qquad [6]$$

$$L_B = \frac{\sqrt{2}\pi}{4} \sqrt[4]{\frac{EI}{\rho_w g D}} \qquad [7]$$

L_B	Ice breaking length that is predicted by the static solution of beam on elastic foundations
E	Young's modulus of the ice
I	Area moment of the beam's cross sectional area
ρ_w	Water density
g	Gravitational acceleration
D	is the width of the beam, taken as 1 here

The mean value and maximum value of each section in the ice penetration domain is separated and illustrated in Figure 9.

The temporal evolution trend of the mean ice load is shown in Figure 9 (a). The general trend of the mean load is increasing from an initially very small load to remaining at a certain higher load level. The mean load may decrease during the interaction, but it can travel back to its previously maintained level immediately. However, for the maximum load in each section, as shown in Figure 9 (b), apart from an initially increasing trend, some decrease of maximum load are also frequently observed. Especially for test 2210 where the 'box' has been pushed through an exceptionally longer distance (20 metres) comparing to all the other experiments

(10 metres), the maximum load increases before the first 20 times the ice breaking length, and then starts to decrease gradually.

Discussions about ice load's temporal variation

As the ice penetration length increases, greater amount of rubble is accumulated in front of the structure (Serré et al., 2013b). Therefore higher ice rotating load and rubble buoyancy would be applied onto the sloping surface. This might be the reason that the mean load is increasing gradually from an initially smaller load value. On the other hand, quite often the maximum load is related to the ice breaking load, which also increases with the rubble accumulation (Lu et al., 2013b). However, when there is sufficient amount of rubble accumulated in front of the structure, the incoming level ice will fail against the piled rubble instead of onto the structure (see Figure 4 (c)). This will bring a decrease on the ice breaking load and hence the recorded maximum load might start to decrease when the ice penetration reaches certain values as shown in Figure 9 (b).

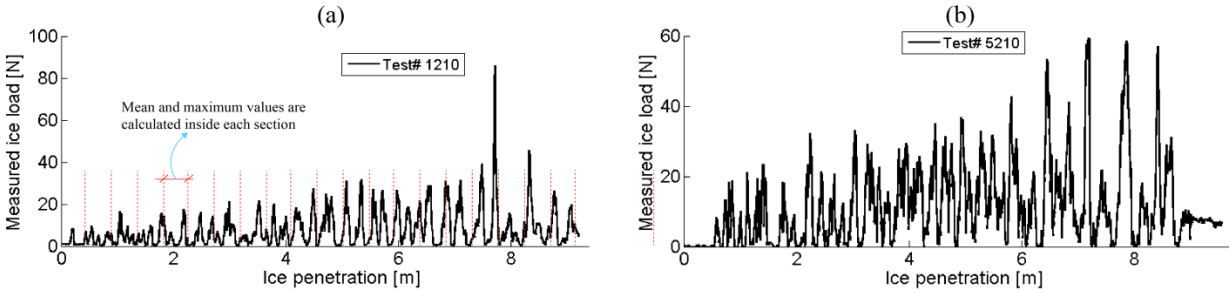

Figure 8 Total measured loading history on the tactile sensor in (a) test1210 and (b) test 5210

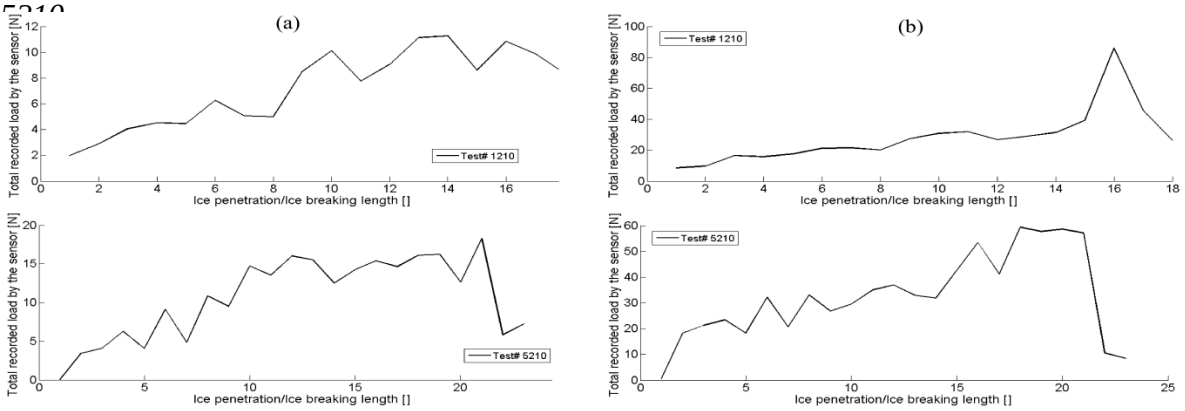

Figure 9 (a) Mean load (left column) and (b) maximum load (right column) of each section in the ice penetration domain.

The above discussion is based on the mean and maximum values within each section of the total ice load history. And the size of each section is chosen as the ice breaking length L_B. The reason that this calculated ice breaking length is chosen as the basis value for separating the ice penetration domain is due to the assumption that a complete interaction procedure can be capsulated in the structure's travelling distance of an ice breaking length. This is to say, as the structure penetrated into the ice for the distance of one ice breaking length, the process of breaking the ice and rotating the broken ice would be complete. In reality the ice breaking length is much smaller than the static prediction of an elastic-foundation beam. A theoretical study in (Lu et al., 2013a) shows that the actual ice breaking length is approximately 1/3 of the static prediction made in Equation [7]. The selected bin length as L_B therefore ensures more than one loading events taking place in each separated section. Choosing a smaller section length would lead to more load history variation in the ice penetration domain and

hence the comparisons become less illustrative. Although the above observation and explanation are rather qualitative, it can help to understand the interaction mechanisms.

Ice load's spatial and temporal variation

In the previous two sections, the measured ice load's spatial and temporal variations were presented and discussed separately. In this section, both the spatial and temporal variation will be presented in a similar fashion. Spatially, the vertical (Z or *i*) direction variation of the load will be accounted for. In the vertical direction, a total of 44 measured values are available in each scan. However, for illustrating purpose, these 44 values are averaged into 11 bins representing the load variation in the vertical direction. Temporally, similarly as in the previous section, the ice penetration history is separated into sections with the length of an ice breaking length L_B. The mean ice loads in different vertical locations were calculated within each section. Thereafter, the spatial and temporal variations of ice load are condensed in the following Figure 10 for test 1210 and test 5210 as an example.

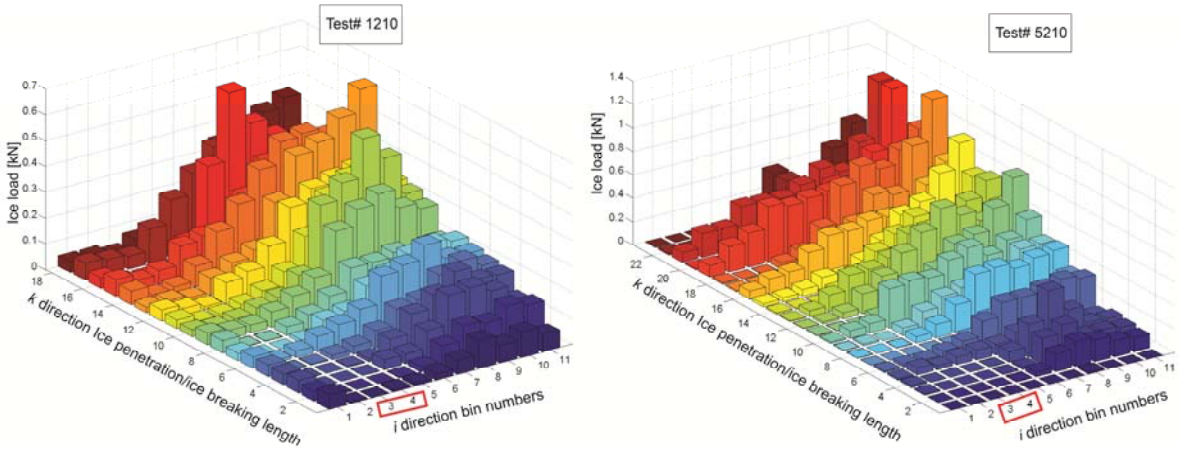

Figure 10 Vertically spatial and temporal distribution of ice load (bins 3 and 4 in the red square is appoximately where the undeformed level ice is).

It can be seen from Figure 10 that generally most of the recorded loads in the vertical *i* direction increase with the ice penetration in *k* direction. This signifies the importance of rubble accumulation. Moreover, below the un-deformed level ice's thickness region (i.e. below bin number 3 and 4 in the *i* direction), the recorded ice load also increases with time and may become even more significant than the process that occur at the un-deformed level ice's thickness region. This further strengthens the point made in the previous section that the accumulated rubble together with the ice rotating process intensifies the ice load under the un-deformed level ice's thickness region.

Conclusion

In this paper, experiments are described to explore the mechanism of level ice interacting with wide sloping structures. In the tests, the tactile sensor has been utilized to measure the spatial and temporal variation of ice load.

Based on the measured load's spatial and temporal analysis, the following conclusion can be made.

- During the interaction, after the breaking of an initially intact ice, the recorded ice load does not diminish instantly. Instead, the ice moves down continuously with a relatively lower load magnitude. This is considered due to the effect of ice rotating load in combination of the accumulated rubble effects;

- Non-uniform contact during ice and wide sloping structure interactions are a rule rather than an exception. This is speculated mainly due to the boundary effects from the confining vertical wall. In reality, the boundary condition may be more complicated and non-stationary (i.e. different boundary conditions in different time). Therefore, different from the current tests where the large loads were deterministically determined at the same place (i.e. both sides in the lateral direction), in reality, the non-uniform lateral load might be randomly non-uniform;
- Based on the mean ice load's (i.e. averaged in time) vertical variation, it is found out that equally large ice load can be detected beneath the un-deformed level ice's thickness region. As discussed above, the contribution of this large ice load is mainly due to the combined effects of ice rotating load and the rubble accumulation;
- Generally the recorded maximum load acts at the un-deformed level ice's thickness region. The ice breaking occurs mainly at the waterline region. This is in line with previous experiments and assumptions that the ice breaking load is one of the decisive loads during design. However, it should bear in mind that that such maximum load detected at the un-deformed may not 100% due to the ice breaking load.

Acknowledgement

The authors would like to acknowledge the Norwegian Research Council through the project 200618/S60-PetroRisk and the SAMCoT CRI for financial support and all the SAMCoT partners. The work described in this publication was supported by the European Community's 7th Framework Programme through the grant to the budget of the Integrated Infrastructure Initiative HYDRALAB-IV, Contract no. 261520. The financial support from Statoil AS and the experimetenal designs of MultiConsult are also greatly acknolwedged. The authors would like to thank Dr. Basile Bonnemaire, Mrs, Oda S. Astrup, Mr. Henning Helgøy, Mr. Sergey A. Kulyakhtin, Mrs Juliane Borge and Mrs Trine Lundamo for great help during the experiments. The authors would also like to thank the Hamburg Ship Model Basin (HSVA), especially the ice tank crew, for the hospitality, technical and scientific support and the professional execution of the test programme in the Research Infrastructure ARCTECLAB.

Reference

Izumiyama, K., Wako, D. and Uto, S., 1999. Ice force distribution on a flat indentor, Proc. of the 14 th Int. Symp. on Ice, Edited by T. Shen, pp. 917-922.

Kim, E., 2012. Personal communication: Saturation pressure. In: w. Lu (Editor), Trondheim.

Kotras, T.V., 1983. Predicting ship performance in level ice. SNAME Trans, 91: 329-349.

Lindqvist, G., 1989. A straightforward method for calculation of ice resistance of ships, Proceedings of POAC 1989, pp. 722-735.

Lu, W., Lubbad, R., Hoyland, K. and Løset, S., 2013a. Physical and theoretical model to study level ice and wide sloping structure interactions (in press). Cold Regions Science and Technology.

Lu, W., Lubbad, R., Serré, N. and Løset, S., 2013b. A theoretical model investigation of ice and wide sloping structure interactions, Proceedings of the 22nd International Conference on Port and Ocean Engineering under Arctic Conditions, Espoo, Finland.

Määttänen, M., Løset, S., Metrikine, A., Evers, K.-U., Hendrikse, H., H, H., Lønøy, C., Metrikin, I., Torodd, N. and Sergiy, S., 2012. Novel Ice Induced Vibration Testing in a Large-scale Facility: Deciphering Ice Induced Vibrations, Part 1, 21st IAHR

International Symposium on Ice. Dalian University of Technology, Dalian, China, pp. 946-958.

Paavilainen, J. and Tuhkuri, J., 2013. Pressure distributions and force chains during simulated ice rubbling against sloped structures. Cold Regions Science and Technology, 85(0): 157-174.

Serré, N., Høyland, K.V., Lundamo, T., Bonnemaire, B., Evers, K.-U. and Gürtner, A., 2013a. Rubble Ice transport on Arctic Offshore Structures (RITAS), part I: Scale-model investigations of level ice action mechanisms, Proceedings of the 22nd International Conference on Port and Ocean Engineering under Arctic Conditions, Espoo, Finland.

Serré, N., Lu, W., Høyland, K.V., Bonnemaire, B., Borge, J. and Evers, K.-U., 2013b. Rubble Ice Transport on Arctic Offshore Structures (RITAS), part II: 2D model scale study of the level ice action, Proceedings of the 22nd International Conference on Port and Ocean Engineering under Arctic Conditions, Espoo, Finland.

Sodhi, D.S., 2001. Crushing failure during ice–structure interaction. Engineering Fracture Mechanics, 68(17–18): 1889-1921.

Sodhi, D.S., Takeuchi, T., Nakazawa, N., Akagawa, S. and Saeki, H., 1998. Medium-scale indentation tests on sea ice at various speeds. Cold Regions Science and Technology, 28(3): 161-182.

Tekscan, I., 2003. I-can Equilibration and Calibration Practical Suggestions. Tekscan, Inc, South Boston, MA.

Tekscan, I., 2011. I-Scan User Manual. Tekscan Inc, South Boston, MA.

Timco, G., 1991. The vertical pressure distribution on structures subjected to rubble forming ice, 11th International Conference on Port and Ocean Engineering under Arctic Conditions, St.John's, Canada, pp. 185-197.

Valanto, P., 2001. The resistance of ships in level ice. SNAME, 109: 53-83.